ACS NANO

www.acsnano.org

ARTICLE

Confined, Oriented, and Electrically Anisotropic Graphene Wrinkles on Bacteria

Shikai Deng,[†] Enlai Gao,[‡] Yanlei Wang,[‡] Soumyo Sen,[§] Sreeprasad Theruvakkattil Sreenivasan,[∥] Sanjay Behura,[†] Petr Král,[§,⊥] Zhiping Xu,[‡] and Vikas Berry*[,†]

[†]Department of Chemical Engineering, University of Illinois at Chicago, 810 S. Clinton Street, Chicago, Illinois 60607, United States

[‡]Applied Mechanics Laboratory, Department of Engineering Mechanics, Tsinghua University, Beijing 100084, China

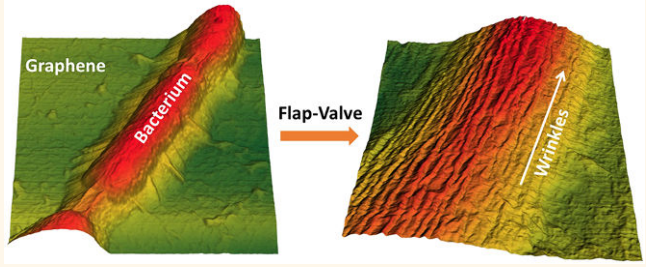
[§]Department of Chemistry, University of Illinois at Chicago, 845 West Taylor Street, Chicago, Illinois 60607, United States

[∥]Department of Automotive Engineering, Clemson University, 4 Research Drive, Greenville, South Carolina 29607, United States

[⊥]Department of Physics and Biopharmaceutical Sciences, University of Illinois at Chicago, 845 West Taylor Street, Chicago, Illinois 60607, United States

Supporting Information

ABSTRACT: **Curvature-induced dipole moment and orbital rehybridization in graphene wrinkles modify its electrical properties and induces transport anisotropy. Current wrinkling processes are based on contraction of the entire substrate and do not produce confined or directed wrinkles. Here we show that selective desiccation of a bacterium under impermeable and flexible graphene *via* a flap-valve operation produces axially aligned graphene wrinkles of wavelength 32.4−34.3 nm, consistent with modified Föppl−von Kármán mechanics (confinement ∼0.7 × 4 μm^2). Further, an electrophoretically oriented bacterial device with confined wrinkles aligned with van der Pauw electrodes was fabricated and exhibited an anisotropic transport barrier (ΔE = 1.69 meV). Theoretical models were developed to describe the wrinkle formation mechanism. The results obtained show bio-induced production of confined, well-oriented, and electrically anisotropic graphene wrinkles, which can be applied in electronics, bioelectromechanics, and strain patterning.**



KEYWORDS: *graphene, bacteria, anisotropy, wrinkles, flap-valve, bioelectromechanics*

Ultrathin, flexible, two-dimensional nanomaterial (2DN) sheets,[1] such as graphene, boron nitride, and transition metal dichalcogenides (MoS_2, WS_2, *etc.*), can form wrinkles,[2] crumples,[3] and folds.[4] These corrugations[5] in free graphene result in local strain distribution and curvature-induced rehybridization of the π-cloud, which modify (a) the electronic structure,[6,7] local charge distribution,[8] dipole moment,[9] and optical properties[3] of graphene and (b) its local chemical potential due to the formation of electron−hole puddles.[10] These modified electrical properties can then be applied toward electronics, self-assembly of complex structures, nanoelectromechanics, and bioelectronics. However, confined and directed wrinkle formation in 2DNs is still a challenge. Here, this challenge was addressed by employing a bacterial cell as a contractible scaffold that can be deposited at specific locations *via* electrophoresis and where graphene deposited atop can form wrinkles.

Integrating the properties of 2DNs with the functionalities of interfaced biological components has produced advanced bionanotechnologies in sensing,[11,12] bioactuated devices,[13,14] and biogated field-effect-transistors (FETs).[15,16] Most of these efforts have focused on electrochemical devices on supported (nominally flat) graphene. Since graphene's electrical properties are sensitive to its morphology (as mentioned above),[6,7] mechanical actuation by the cell of the interfaced graphene can produce wrinkled graphene with modified properties. We employ rod-shaped *Bacillus subtilis* cells for this work for their following attributes: (i) nominally rod-shaped (orientable), (ii) size of 1 × 5 μm^2 (can produce confined wrinkles), (iii) long and connected chain forming bacteria (for longer wrinkles), and (iv) highly volatile intracellular content (∼75−80% water) (shrinkable: cell contracts with water reduction). Our previous work showed that graphene atop a cell retains its aqueous content under high vacuum enabling wet microscopy.[17] Here, we designed a graphene flap-valve *via* interaction of monolayer graphene with a biological cell (*B. subtilis*), which permanently removes the bacterium's aqueous content under vacuum (Figure 1a). This mechanism introduces compressive strain to form axially aligned wrinkles on graphene. As will be shown

Received: May 14, 2016
Accepted: July 8, 2016
Published: July 8, 2016

© 2016 American Chemical Society

DOI: 10.1021/acsnano.6b03214
ACS Nano 2016, 10, 8403−8412

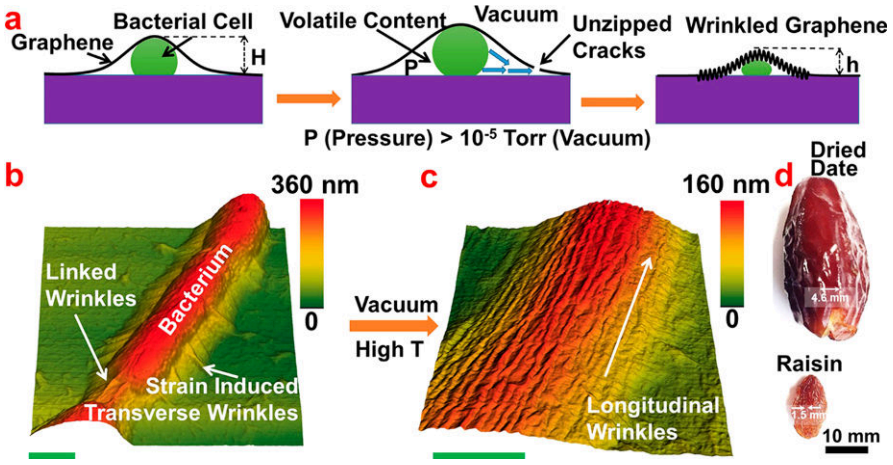


Figure 1. Schematic of the graphenic wrinkle-formation mechanism *via* graphene flap-valve-induced permanent shrinkage of the interfaced bacterium. (a) Cross-sectional model of the graphene-covered bacterium sample, which under vacuum bulges and undergoes unzipping. The graphene then acts as a flap-valve to remove the aqueous content of the bacterium, subsequently contracting it to produce wrinkles (10^{-5} Torr and 250 °C). (b, c) 3D AFM surface morphology images of graphene on a bacterium before (b) and after (c) heat/vacuum treatment. The wrinkles (λ = 32 nm) formed are longitudinal and clearly visible. The scale bars in (b) and (c) are 0.5 μm. (d) Longitudinal wrinkles on the skin of a dried date (λ = 4.6 mm) and a raisin (dried grape) (λ = 1.5 mm).

later, we electrophoretically assembled a bacterium aligned with electrodes to achieve graphene wrinkles with controlled orientation.

Freshly cultured (in nutrient broth) and washed (in deionized water) Gram-positive *B. subtilis* cells were immobilized on SiO_2-coated Si substrates, followed by the transfer of a monolayer graphene sheet synthesized *via* chemical vapor deposition (CVD); see details in the Materials and Methods section. This was followed by application of heat (~250 °C) and vacuum (10^{-5} Torr) treatments to vaporize the bacterium's volatile components and subsequently to apply pressure on graphene for creation of unzipped cracks[18] (Figure 1a). Since graphene is impermeable[19] and strong,[20] this crack creates a pathway for volatile cellular content to escape. However, the graphene's "flap-valve" operation inhibits bacterial reswelling, causing the bacterium to shrink permanently. This phenomenon is attributed to the opening of an impermeable graphene flap on the SiO_2/Si substrate when pressure $P_{inside} > P_{outside}$, where the pressure difference drives the water out, and to the closing (sealing graphene on SiO_2) of the graphene flap when $P_{inside} < P_{outside}$ (*via* adhesion with the substrate) to reject any intake. Further, the removal of intracellular content caused (energetically favored) radial shrinkage of the bacterium (minimal axial shrinkage)[21] and the creation of longitudinal wrinkles. The interplay between the bending stiffness of the interfaced free graphene sheet and the compressive stress from the adhered bacterium cell wall (shown later) results in the formation of wrinkles (as described by the Föppl–von Kármán equation). The wrinkle formation continues until the volatile content is evacuated out of the bacterium.

RESULTS AND DISCUSSION

The wrinkle pattern and the thickness of the shrunk graphene–bacterium system remain unchanged even after immersion in water for several days or exposure to a humid environment (Figure 2g). The operation of this one-way flap-valve is comparable to shrink wrapping and a check valve (for example, a Ziploc vacuum bag's one-way valve (see Supporting Movie S1)). In contrast, the native bacterium without graphene and after desiccation (control samples) swells up instantaneously when immersed in water for 5 s and gradually increases under atmospheric humidity (Figure 2g).

Before shrinkage and flap-valve operation, radial (transverse) wrinkles on graphene (about 500 nm of length and 70 nm of width) are produced. These are attributed to its Poisson's ratio (ν = 0.165 = $-\varepsilon_y/\varepsilon_x$).[2,3] Here, graphene's interaction with the additional perimeter of the protruded curved bacterium causes graphene to undergo tensile strain (mostly in the radial direction). This leads to graphenic compression in the axial/longitudinal direction (due to the Poisson's ratio), forming the radial wrinkles (Figure 1b).

The graphene wrinkles formed are longitudinal and confined atop the bacterial cells (and sometimes connected between neighboring cells) as observed under field emission scanning electron microscopy (FESEM) as shown in Figure 2. Since the FESEM micrograph contrast corresponds to electron scattering due to surface curvature (as on wrinkles) and electron density,[22] the contrast pattern (inset of Figure 2) provides the number of wrinkles (n) on each transverse bacterium with an average wavelength, λ (distance between two wrinkles), of 32.4 ± 3 nm (see Supporting Information Section 2 for calculation details).

The wrinkle wavelength is independent of the diameter of the bacteria, since (a) the wrinkle wavelength is a consequence of the balance of graphene's bending energy and the bacterium's contraction energy, both of which are relatively unaffected by the bacterial diameter, and (b) the bacterial curvature is significantly smaller than the wrinkle curvature ($D_{bacteria}/\lambda_{wrinkle}$ = 20–35) to have a significant geometric effect on the wrinkle wavelength (as shown in Supporting Figure S3). The angular image analysis depicts[23] that the texture direction (TD) of the selected wrinkle area is 89.7 ± 0.6° (close to 90°) (Figure 2b), implying longitudinal directionality of wrinkles. Further, a surface with a texture aspect ratio (TAR) of 0.125 (<0.3) (Figure 2c) for the wrinkled graphene indicates strong spatial anisotropy.

The atomic force microscope (AFM) scans of graphene interfaced with bacteria after vacuum and heat treatment as shown in Figure 2d and e are consistent (wavelength = 34.3 ± 2 nm) with FESEM image analysis in Figure 2a (additional

DOI: 10.1021/acsnano.6b03214
ACS Nano 2016, 10, 8403–8412

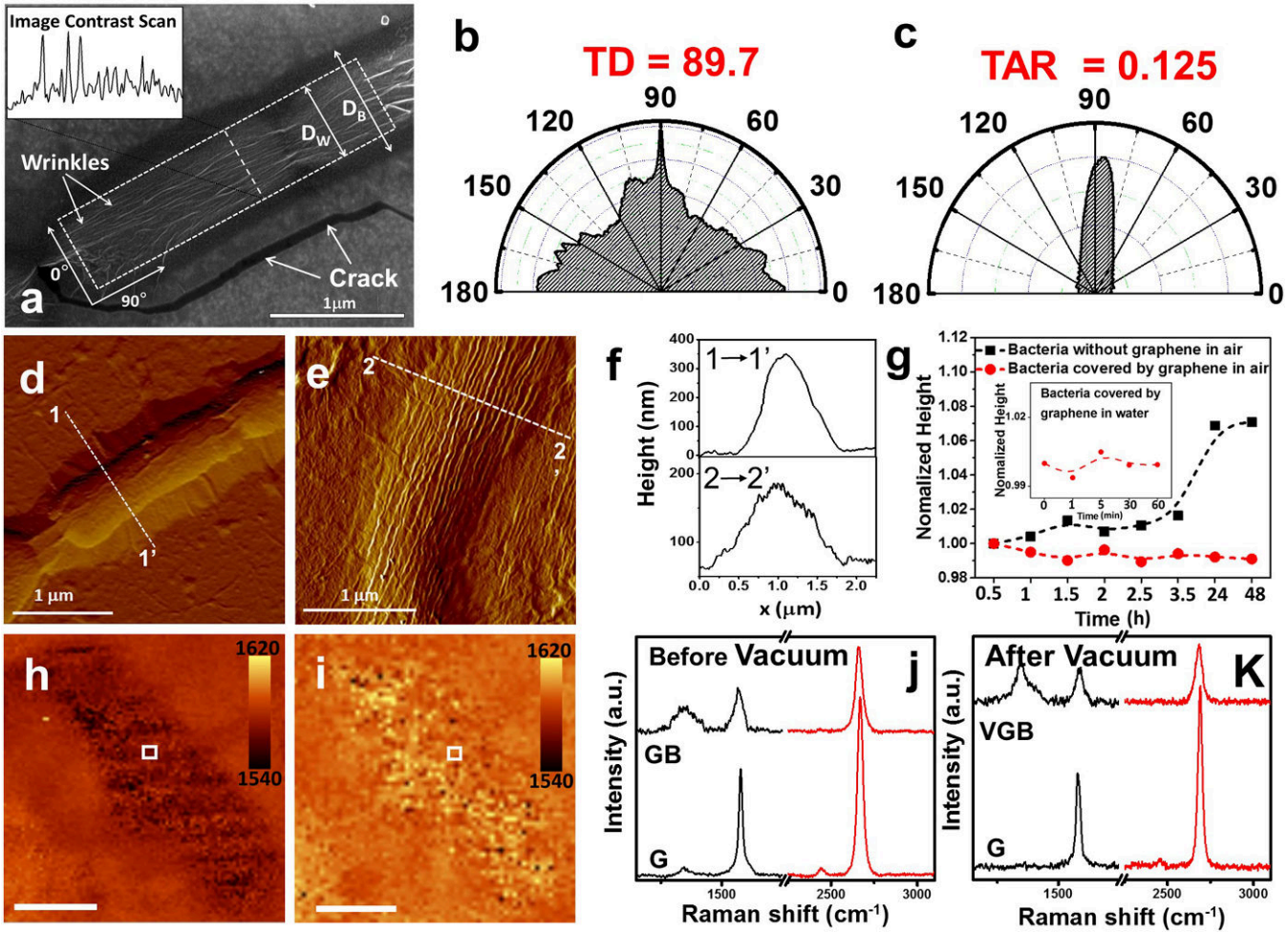


Figure 2. Wrinkles on graphene. (a) FESEM image of one and a half bacteria. The inset is the brightness contrast scan; D_B is the diameter of the bacteria and D_W is the diameter of the wrinkle area within the bacteria range. (b) Texture direction *Std* image of the dashed-line rectangle in (a). (c) Texture aspect ratio parameters, *Str37* image of the dashed-line rectangle in (a). AFM topography of graphene on the bacterium before (d) and after (e) vacuum and temperature treatment. (f) Height profiles corresponding to the white dashed line in parts (d) and (e), respectively. (g) Temporal study of bacteria height in air after vacuum. Bacteria not covered by graphene (black dash−square line), bacteria covered by graphene (red dash−circle line); (inset) bacteria covered by graphene in water after vacuum. G peak position mapping of graphene-on-bacteria surface before vacuum (h) and after (i). (j) Raman spectra of graphene on a SiO_2/Si substrate (G) and of graphene-on-bacterium (GB) before vacuum: white square shown in panel (h). (k) Raman spectrum of graphene on a SiO_2/Si substrate (G) and of graphene-on-bacterium after vacuum (VGB): white square shown in panel (j). Scale bars in (h) and (i) are 1 μm.

AFM results shown in Figure S4 and wavelength calculation details outlined in Supporting Information section 1 and Figures S5 and S6). The height of the wrinkles varies from 7 to 10 nm. Unlike FESEM, which operates under high vacuum, AFM allows inspection under atmospheric pressure (Figure 2). Post-vacuum/heat treatment, the AFM micrographs obtained under atmospheric pressure continue to show wrinkles on graphene (even after several days), which implies that the aqueous content is permanently lost and does not reenter the (highly hygroscopic) bacterial cells.

The relative strain on graphene at different stages of the graphene−bacteria interaction was investigated *via* Raman shift measurements of the G and 2D peak positions as well as their shapes.[24] The elongation and weakening of the C−C bonds lead to a Raman red-shift (lowering of the vibrational frequency). The peak's full width at half-maximum (FWHM) increases upon application of tensile stress.[25] The Raman mapping of graphene on the bacterial surface before and after vacuum treatment is displayed in Figure 2h and i, respectively. Both the G and 2D peak positions of graphene on the bacterium's surface (Figure 2j and k and Figure S8) are red-shifted compared to graphene on a flat substrate (darker on the bacterium than on SiO_2), indicating the existence of tensile strain induced by bacterial curvature (FESEM and AFM).[24] The strain also increases the FWHM of the G peak from 15 cm^{-1} to 33 cm^{-1} (more than 2-fold). After vacuum/heat annealing and wrinkle formation, graphene on bacteria exhibits a blue-shift in the G peak with respect to graphene on SiO_2/Si (brighter on the bacterium than on SiO_2/Si). This Raman blue-shift can be attributed to the release of tensile strain or addition of compressive strain due to the formation of wrinkles. Further, the entire graphene region exhibits a blue-shift (~15 cm^{-1} increases in G and 2D peak positions) attributed to desorption of O_2 and other adsorbents.[26] The 10 cm^{-1} red-shift of the 2D peaks implies a strain of 0.37% for graphene on the bacterium[27] (see the Supporting Information, Section 4). Studies with other cell types and strains are important; however these are beyond the scope of the current work.

DOI: 10.1021/acsnano.6b03214
ACS Nano 2016, 10, 8403−8412

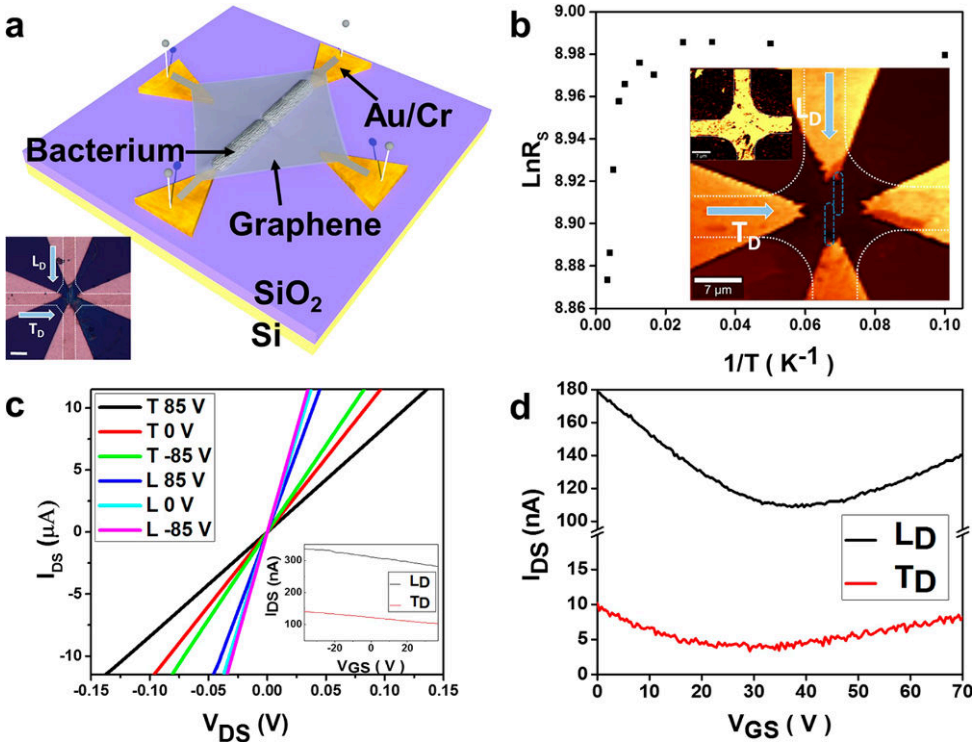


Figure 3. Longitudinal and transverse carrier-transport measurements of wrinkled graphene on bacteria. (a) Schematic of graphene on a bacteria FET device and a typical optical image of the device design after graphene placement *via* electrophoretic deposition with a subsequent lithography technique: longitudinal direction (L_D) and transverse direction (T_D) are depicted with arrows. The scale bar is 10 μm. (b) Activation energy: resistances (at gate voltage of 85 V) at different temperatures were measured to determine the activation energy of carrier transport. The inset figure shows Rayleigh scattering mapping of the device; inset figure is Raman intensity mapping of the graphene 2D peak. (c) Drain−source current (I_{DS}) *vs* drain−source voltage (V_{DS}) study at 10 K for L- and T-directions at different gate voltages, showing the higher conductivity in the L-direction. Inset shows the FET characteristics of drain−source current (I_{DS}) *vs* the gate−source voltage (V_{GS}) at 1 mV (V_{DS}). (d) FET transport characteristics of I_{DS} *vs* V_{GS} at 10 K with a clear demonstration of Dirac points.

In order to study the effect of graphenic wrinkles' orientation on the carrier transport, we fabricated a "plus-shaped" wrinkled-graphene-on-bacterium device (van der Pauw structure) with bacteria placed parallel and perpendicular to a pair of respective electrodes (Figure 3a). The FESEM and AFM micrographs confirm that the graphene wrinkles are oriented in the longitudinal direction. The Raman scan images clearly show that graphene stays atop Au/Cr electrodes after wrinkle formation, and there is no separation of graphene from the electrodes. The transverse length (or width) of graphene on bacteria is about 1 μm and on SiO_2 is 9 μm with excess graphene on the Au/Cr electrodes. Therefore, if there is any contraction causing graphene to slide, there will be excess on the electrode.

Current−voltage (I−V) characteristics under vacuum exhibited lower conductivity in the transverse direction (T-direction) than in the longitudinal direction (L-direction) (at all applied gate voltages). Out of the 10 devices tested, the doping levels were varied and the Dirac point (with p-doping) was observed for only two devices (Figure 3d). At respective Dirac points (zero net doping, n = p), the conductivity in the L-direction was higher than that in the T-direction. Further, the Dirac point for L-transport was ∼8 V higher than that for T-transport, or in other words, L-transport had more holes (<1.46 × 10^4 holes/μm^2 (as carrier concentration $n = 2C_{SiO2}\Delta V/e$)). This represents the difference in the participating doped charges from bacteria along the two conduction pathways: The least resistive path in the L-direction has more bacteria (thus more doping) than in the T-direction. This also explains the sharper Dirac point in the L-direction (Figure 3d). Clearly, the bacterium significantly p-dopes the overlaying graphene sheet. It is important to note that the net gate capacitance will include the capacitance from SiO_2 and the bacterial dielectric ($C_{gate\text{-}net}^{-1} = C_{SiO2}^{-1} + C_{bacterium}^{-1}$). The other eight devices exhibited reduction in current with increase in gate voltage from −85 to +85 V (Figure 3c) for temperatures ranging from 10 to 300 K (beyond 85 V, dielectric breakdown started). The variation in the overall doping is attributed to bacteria of different ages having different surface potentials.[28]

To determine the transport activation barrier, temperature studies were conducted at reduced doping levels at the maximum gate voltage (85 V) (Figure 3b). Two conduction regimes were identified: (i) high temperature (120 to 300 K) and (ii) low temperature (10 to 120 K). The activation energy ($I \propto \exp(-E_A/kT)$) for the high-temperature regime in the T-direction was 1.69 ± 0.01 meV higher than that in the L-direction. The Schottky barriers at the electrode−graphene junctions are expected to be similar for L- and T-transport, indicating a slightly increased barrier for transverse transport. Note that the barrier must not be affected by the carrier concentration. Therefore, the anisotropic wrinkles lead to suppressed carrier mobility in the T-direction.[4] This is speculatively attributed to the additional barrier due to local charge concentration distribution (and potential distribution) following the pattern of the longitudinal wrinkles (for example, electron−hole puddles may be patterned *via* the wrinkles).

DOI: 10.1021/acsnano.6b03214
ACS Nano 2016, 10, 8403−8412

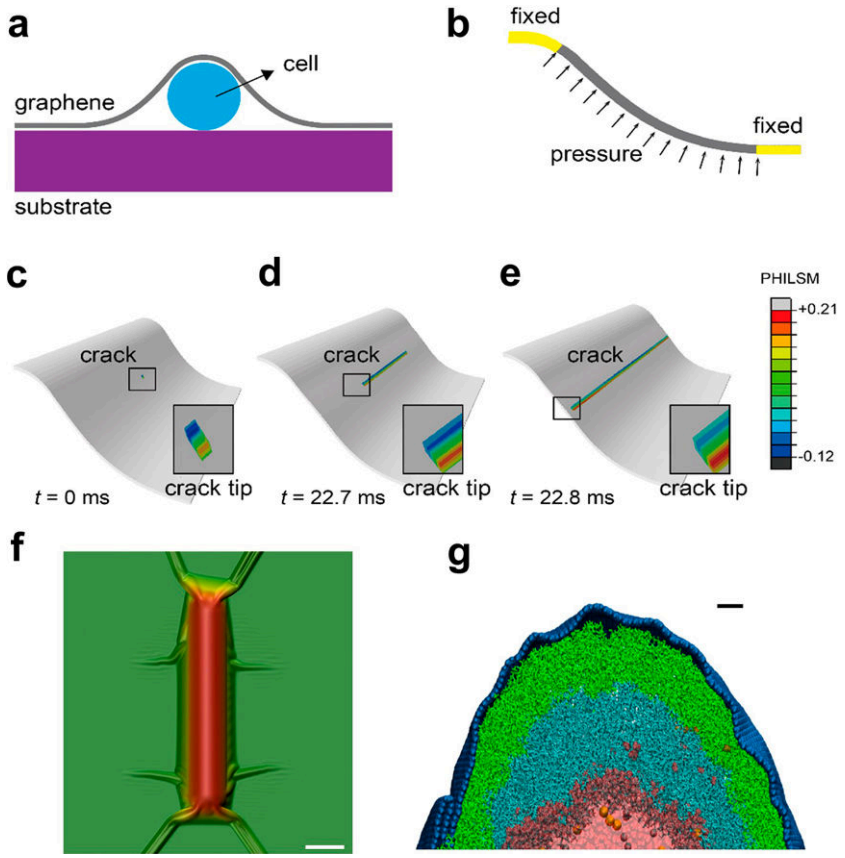


Figure 4. Extended finite element method simulations (XFEM), coarse-grained molecular dynamics simulations (CGMD), and atomistic molecular dynamics simulations. (a) Illustration of graphene-on-bacteria cell-on-SiO_2/Si model, where the configuration of graphene is obtained from CGMD simulations. (b) Loading condition of graphene in our XFEM simulations. (c–e) Development of cracks in graphene at time t = 0, 22.7, and 22.8 ms. The insets show PHILSM contours of the crack tip at different times in response. The factor PHILSM is a signed distance function to describe the crack surface, which is used to indicate the crack location. (f) CGMD simulation of bacteria covered by graphene before vacuum annealing. Bacteria covered by graphene, where wrinkles are developed in the radial directions to the pretension induced by adhesion from the substrate and bacteria. The scale bar is 1 μm. (g) Atomistic molecular dynamics simulations of a single peak of wrinkles on a desiccated bacterium covered with graphene. Blue layer represents the graphene layer, green layers represent peptidoglycan, and cyan layers represent the bacterial lipid bilayer. Pink spheres represent water molecules, sodium ions are represented by yellow spheres, and chloride ions are shown by cyan spheres. Scale bar is 1 nm.

Further, since for folds the T-conductivity is expected to be higher,[4] it confirms that this is a wrinkle-intensive device. Also, at reduced temperature, the thermal expansion of graphene is expected (−ve thermal expansion),[2] which might lead to relaxation of wrinkles. This is consistent with the significantly reduced activation energy for the low-temperature regime. Further work is required to obtain measurements by using a different cell (for example, noncharged Gram-negative cell with no peptidoglycan membrane) to study the modification in the band structure of wrinkled graphene.

Mechanisms of Graphene–Bacteria Interaction. To understand the mechanism on free graphene interfaced with a biological cell, coarse-grained molecular dynamics (CGMD) simulations were performed. Here, the graphene sheet is pulled by the curved bacterium, creating transverse wrinkles (Figure 1b) (see Supporting Movie S2). Clearly, the presence of radial wrinkles implies pretension in the graphene membrane on the bacterium.[29,30] We also studied in-plane strain along the cross-section profile of graphene/bacterium contact as 0.42 ± 0.01% in the CGMD simulations, which is in good agreement with strain measured *via* Raman spectroscopy. Post-vacuum/heat treatment, the size of the bacterium model was set to shrink by 40%, consistent with the experimental conditions. The simulation incorporated the structural relaxation after shrinking, which results in the generation of wrinkles on graphene on the bacterial surface. The process starts from nucleation of wrinkles with small wavelengths and continues by merging of a converged configuration with stabilized wavelength that is defined by the amplitude of shrinking as well as the elasticity of the bacteria and graphene (as shown in Figure S10 and Supporting Movie S3). The stabilized wavelength of wrinkles predicted using the physical parameters for the system is about 34 nm, which is also consistent with the measured average wrinkle wavelength (simulation details and parameters are provided in the Supporting Information).

The crack formation on graphene under heat and vacuum treatment is attributed to two mechanisms: (a) opposite polarity of thermal expansion coefficients between the graphene (−ve thermal expansion coefficient) and bacteria (+ve thermal expansion coefficient)[31] and (b) radially induced tensile stress due to the applied pressure from volatile bacterial content (estimated to be ∼100 bar; see Supporting Information). The region where graphene transitions from the bacterium to the SiO_2/Si substrate experiences a high differential strain due to a change in curvature (bacterium−SiO_2/Si boundary) and high tensile stress due to the large pressure difference across

DOI: 10.1021/acsnano.6b03214
ACS Nano 2016, 10, 8403–8412

graphene (pressurized volatile cellular matter to vacuum). The tensile strain causes longitudinal crack nucleation at the inflection points near the substrate, as shown by extended finite element method (XFEM) simulations: the crack is formed perpendicular to the stress direction (Figure 4e and Supporting Movie S4). The width of the cracks (speculatively zigzag edged) was mostly independent of the bacterial size at about 200 nm. In some cases, the graphene/bacteria system under vacuum did not have to be heated to form cracks (attributed to defects on graphene), which were always on the bacterium/substrate interface. It should be note that cracks formed only on graphene-wrapped immobile bacteria on the substrate but not on graphene-wrapped free-standing bacteria, as shown in Figure S11.

We also performed atomistic molecular dynamics simulations to better elucidate the interface and adhesion between graphene and the bacterial cell wall for a single-wrinkle peak (17 nm wide, similar to the experimental results, shown in Figure 4g and Figure S11) on bacteria covered with graphene. The simulated system consists of graphene interfaced with the bacterial cell wall: peptidoglycan layer (thickness 25−30 Å, 100 × 600 Å^2), lipid bilayer (80 × 550 Å^2), cytosol (protein, 0.18 M ions and hydrating water) and water layer, from top to bottom, respectively. The simulation detail is described in the Supporting Information. The simulation clearly shows that graphene stays strongly adhered to the bacterium cell wall, implying a high adhesion energy (calculated 218 mJ/m^2 in comparison to 288 mJ/m^2 for graphene on SiO_2 as shown in the Supporting Information). Further, small folds within the wrinkle were also observed (however, not resolved by experiments).

The morphology correlates with a Young's modulus of the substrates. Micro- and macroscopic wrinkles are ubiquitous in clothes, leaves, animal skins, dried fruits (raisins, dates (Figure 1d)) and other surfaces. Nanoscale wavelengths require ultrathin skin as per the Föppl−von Kármán relationship:[32]

$$\lambda = 2\pi t\left(\frac{\bar{E}_{2DN}}{3S\bar{E}_S}\right)^{1/3} \quad (1)$$

where λ is the wrinkle wavelength, t is the thickness of the 2DNs, $\bar{E}_{2DN}$ is the plane-strain modulus of the 2DNs film, and $\bar{E}_S$ is the in-plane strain modulus of the substrate. $\bar{E} = E/(1 - \nu^2)$, where E is Young's modulus and ν is Poisson's ratio. Equation 1 assumes a strong adhesion between 2DNs and the substrate with no slip between the two layers. Since it is the thinnest material, graphene's wrinkle wavelengths are expected to be small. Further, $\lambda_{graphene}$ depends on the strain modulus of the substrate,[33] with stiffer surfaces producing smaller wavelengths. The Young's modulus and Poisson's ratio of graphene are E_g = 1 TPa and ν_g = 0.165, respectively. Equation 1 includes a prestretch factor (S), corresponding to the prestretched substrate:[3]

$$S = (1 + (1 + \varepsilon)^3)/2(1 + \varepsilon) \quad (2)$$

The average amplitude of the wrinkles is

$$A = \frac{\bar{L}t}{\lambda}\left(\frac{8\nu}{3(1 - \nu)^2}\right)^{1/2} \quad (3)$$

From FESEM image analysis, the prestretch factor, S is calculated to be 2.657 (see the Supporting Information, Section 3). Here, A is the amplitude of the wrinkles and $\bar{L}$ is the average length of the wrinkles. The perpendicular stress on the graphene can be estimated by

$$P = \frac{w\bar{E}_S}{2t\left(\frac{\bar{E}_{2DN}}{3S\bar{E}_S}\right)^{1/3}} \quad (4)$$

where w is the perpendicular displacement of the graphene and P is the stress component by the bacterial cell wall acting perpendicularly on graphene (see the Supporting Information).

Combining eq 1 with the experimental wavelength values, we estimate Young's modulus of the bacterial cell wall to be between 35.7 and 42.2 MPa, comparable with other measurements (39 MPa).[34] Further, we calculate the average amplitude of wrinkles as $A = w_{max}$ = 7.3 nm from eq 3, which is also consistent with AFM measurements, and the maximum perpendicular stress (p_{max}) acting on graphene is 40.18 MPa. Further studies are required to understand the effect of other bacteria, such as Gram-negative bacteria. Since for one bacterial cell, the Young's modulus would not change, the wrinkle wavelength is fixed for one cell. The wavelength can be tuned by changing the cell type. The amplitude of the wrinkle is dependent on the shrinkage of the cell. This too can be changed by changing the cell. Therefore, the amplitude or wavelength of wrinkles can be tuned if we use different cell types. Further, graphene wrinkles can be compared with wrinkles on raisins, λ = 1.5 mm (Figure 1), where with the grape skin being 30 times[35] stronger than the grape pulp implies a skin thickness of 111 μm. Remarkably, graphene, being ∼370 000 times thinner than grape skin, is able to retain its mechanical characteristics while interacting with the shrinking bacterium.

CONCLUSIONS

In summary, the bacterium scaffold can be employed to achieve selectively patterned, aligned, confined, and electrically anisotropic graphene wrinkles. This is realized by flap-valve operation of graphene, which functions as a mass-transfer diode. The longitudinal (high-texture aspect ratio) graphenic wrinkles with ultrasmall wavelength (32−34 nm) controllably aligned between electrodes exhibit an anisotropic transport barrier (ΔE = 1.69 meV). This study can be extrapolated for formation of confined wrinkles on other 2DNs and for reduced wrinkle wavelengths *via* bacterial cells with a higher Young's modulus (or *via* hygroscopic polymer patterns). The work could also evolve advances in cytoelectronics and 2D electronic circuitry with controlled wrinkle placement.

MATERIALS AND METHODS

Experimental Process. *Bacteria Preparation.* Rod-shaped, Gram-positive *Bacillus subtilis* bacterial strands (0.5 to 1.5 μm in width and lengths from 1 to 5 μm) were used in this study. *B. subtilis* were grown in agar gel (OXOID CM0003B), and care was taken to ensure that there is no cross-contamination. A pellet of *B. cereus* cells was introduced into 100 mL of nutrient broth solution (0.13 g/mL nutrient broth (OXOID CM0001B) sterilized in an autoclave at 121 °C for 12 min) in an Erlenmeyer flask using a sterilized culture-transfer rod. The flask was sealed with cotton and placed in an incubator to grow the culture at 31.0 °C for 14−15 h (shake frequency = 62 rpm). After the growth period, the bacterial cells were separated from the medium by centrifuging the suspension at 6000 rpm for 10 min and resuspending the pellet in DI water. This was repeated three times to remove the nutrient broth from the bacterial suspension.

Bacteria Deposition on the Silicon Dioxide Surface. A fresh chip (285 nm SiO_2-on-silicon substrate) was sequentially washed with

DOI: 10.1021/acsnano.6b03214
ACS Nano 2016, 10, 8403−8412

acetone, isopropyl alcohol, and DI water and was dried under N_2 flow. The prewashed chip was exposed to oxygen plasma (0.0058 psi, 100 W, 2 min). The chip was then immersed in the bacterial suspension (in DI water) for about 1 h, followed by carefully washing and drying in N_2 flow. This leads to bacterial cells adhering on the SiO_2 substrate by excreting extracellular polysaccharides, which bind them on the surface. Because of washing by DI water, the polysaccharides will not exist on the top surface of the bacteria. The process is shown in Figure S1.

Graphene Growth and Transfer. In this step, a high-quality monolayer graphene sheet is laid on top of the bacterial cells. Here, graphene is grown *via* a CVD process on a copper foil (25 μm) at 1000 °C with purging CH_4/H_2 (20/10 sccm) in a 1 inch quartz tube for 5 min. A layer of PMMA is then spin-coated (20% PMMA at 4000 rpm for 1 min) on graphene (on Cu foil), followed by dissolving the copper foil in 30% nitric acid. The PMMA−graphene composite film that floats on the top was transferred to a water bath to get rid of the acid residues. The film is then carefully transferred onto the bacterial chip prepared in the previous step. This is followed by the removal of the PMMA layer (acetone solution wash, 50 °C for 4−5 min) to produce graphene-wrapped bacteria immobilized on the chip.

Annealing Process. Here, the sample was exposed to vacuum and high temperature to trigger the wrinkle formation process. For this, first, the CVD tube was flushed with H_2 gas (100 sccm) for 15 min. The chip (from step 3 having bacteria covered by graphene) was placed into the vacuum chamber and the temperature was raised to 250 °C. The sample was kept at this condition for 3 h.

Electrophoretic Trapping. A droplet of the diluted bacteria solution (same solution from step 1) is carefully placed in the area between the electrodes with a syringe. These two electrodes were connected to the ac signal source generator (Agilent 33220A) through two metal probes. An ac signal with a peak-to-peak voltage of V_{pp} = 10 V and frequency of f = 5 MHz was applied on the ensemble for 5 to 10 min. The bacterial cells experience a force toward positive field gradient (higher field intensity) and thus are directed toward the electrode junction, where they immobilize, bridging the electrode gap. This is followed by transfer and placement of monolayer graphene atop the bacterial cells.

Photolithography and Device Fabrication. Photoresist was spin coated on the samples at 4000 rmp for 40 s, followed by soft baking at 110 °C for 1 min. Samples are aligned and exposed in an MA6Mask aligner with hard contact for 12 s at 900 W UV power. The exposed samples were developed in developer for 12 s. O_2 plasma exposure was performed on this developed samples to remove the uncovered graphene, followed by immersion in etcher for 5 min. Finally, samples are washed and cleaned in DI water.

Simulation Processes and Parameters. *Coarse-Grained Molecular Dynamics.* Coarse-grained molecular dynamics simulations are performed using the LAMMPS code.[36] We adopt a renormalized hexagonal lattice for graphene with a lattice constant of $a = 300a_G$ and $5a_G$ for the covering and shrinking processes, where a_G is the lattice constant of the full-atom model for graphene. Bond stretching, bond angle bending, and dihedral terms are included to describe the elasticity of the graphene sheet and the bacterial cell membrane. The interaction between graphene, bacteria, and the silica substrate is modeled through the Lennard-Jones formulism for pairwise interaction, *i.e.*, $4\varepsilon[(\sigma/r)^{12} - (\sigma/r)^6]$. The total energy is then written as $E_{tot} = E_G + E_B + E_S + E_D + E_{G\text{-}B} + E_{G\text{-}S}$, where the energy of a bond with length r, bond angle (θ), and dihedral angle (ϕ) terms are calculated as $k_b(r - r_0)^2$, $k_a(\theta - \theta_0)^2$, and $k_d[1 + d\cos(n\phi)]$, respectively. The parameters are fitted to reproduce tensile stiffness, the bending rigidity of graphene and the bacteria membrane, and the adhesion between graphene, the bacterial membrane, and the substrate. The graphene sheet has a Young's modulus of Y = 1 TPa by considering the thickness of graphene as 0.335 nm and a bending rigidity of 1.04 eV, which is calculated from full-atom simulations and consistent with the value reported in the literature.[37] The Young's modulus of the cell membrane is about 30 MPa. The interfacial energy $\gamma_{G\text{-}B}$ for the graphene−bacteria contact is 218.0 mJ m^{-2}, which is calculated from our full-atom MD simulations using the CHARMM force field and is consistent with previous reports for the interface between graphene and the polymer.[38,39] These graphene−bacteria contact MD simulations are performed using the large-scale atomic/molecular massively parallel simulator (LAMMPS) package.[36] The interatomic interactions for graphene are described using the adaptive intermolecular reactive empirical bond order (AIREBO) potential functions with the torsion term and van der Waals interaction included.[40] The CHARMM36 force field is used for the lipid bilayer.[41] The SHAKE algorithm is applied for the stretching terms between oxygen and hydrogen atoms to reduce high-frequency vibrations that require shorter time steps. The interaction between graphene and the lipid bilayer includes both van der Waals and long-range Coulomb interactions. The van der Waals interaction is described by the 12−6 Lennard-Jones potential $4\varepsilon[(\sigma/r)^{12} - (\sigma/r)^6]$ at an interatomic distance r. The van der Waals forces are truncated at 1.0 nm, and the long-range Coulomb interactions are computed by using the particle−particle particle−mesh (PPPM) algorithm.[42] The adhesion energy between the graphene and lipid bilayers is $E_b = ((E_{cell} + E_G) - E_{cell\text{-}G})/A$, where A is the contact area between the graphene and lipid bilayers, and $E_{cell\text{-}G}$, E_{cell}, and E_G are energies of the hybrid system, isolated graphene monolayers, and lipid bilayers, respectively. The value of $\gamma_{G\text{-}S}$ 288 mJ m^{-2} for the graphene−silica substrate contact is taken from the literature.[43,44] The adhesion between bacteria and substrate, which is less relevant to the current problem, is set to the same value for simplicity.

With this definition of E_{tot} as a function of the atomic positions, energy minimization calculations are carried out to relax the microstructures of the hybrid system. The conjugated gradient algorithm is used. In this work, we use different parameters to simulate the process of graphene coating and wrinkle formation caused by the shrinking of the bacteria, because the spatial resolution requirement is much higher in the latter case. To minimize the computational cost after refining the coarse-grained model, we reduce the model to two dimensions—the cross-section plane—as shown in Figure S10b. A periodic boundary condition is implemented along the bacteria axis with a simulation box size of 1.23 nm, which is the coarse-grained lattice constant along the zigzag direction. These two sets of parameters are summarized in Tables S4 and S5.

After graphene wraps the bacterium, a tensile strain will be induced within the sheet due to the interaction with the bacterium. To calculate the strain, we measure the C−C bond length (l_{C-C}) after graphene wraps the bacterium in our CGMD simulation, using eight different simulation snapshots for averaging. In our simulations, the armchair direction of graphene is along the direction of the bacteria. So the projection of the C−C bond in graphene on the direction of bacteria should have two different lengths, l_{C-C1} and l_{C-C2}. The distribution of their values is summarized in Figure S10a, showing two separated peaks corresponding to l_{C-C1} and l_{C-C2}. The projections of the C−C bond length along the direction of the bacterium after wrapping are l_{C-C1} = 0.712 Å and l_{C-C2} = 1.428 Å before the wrapping process. The line in-plane strain ε_l within graphene along the direction of the bacterium induced due to the bacterium/graphene contact during the wrapping can be defined as

$$\varepsilon_l = \left(\frac{\Delta l_{C-C1}}{l_{C-C1}} + \frac{\Delta l_{C-C2}}{l_{C-C2}} \right)/2$$

Extended Finite Element Method Calculations. There is some air remaining under the graphene sheet before annealing, and at 250 °C, some of the organic composition degenerates and releases some gases, such as CO_2, NH_3, and SO_2. Assuming the gas released under vacuum is 1% of the mass of the total liquid phase, the pressure increase under the vacuum environment is from the released gas and vapor steam from water. The volume of the liquid phase (water, bacteria, and other organic compositions) is V_L, and the volume of air is V_A before annealing. Assume the ratio of the liquid phase to air is $c = V_L/V_A$ = 10. The molecular number of the gas phase is $n_G = V_A D_A/M_A$. The molecular number of the gas phase is $n_L = V_L D_L/M_L$. D_A is the density of air, which is 1.27g/L. D_L is the density of the liquid phase; we set it to be the same as water's, which is 1000 g/L. M_A and M_g are

DOI: 10.1021/acsnano.6b03214
ACS Nano 2016, 10, 8403−8412

molecular masses of the gas and released gas mixture; both of them are 29. The volume of the total gas phase (V_g) may increase twice under vacuum before crack formation compared with that (V_A) in atmospheric pressure (P_A).

$$n_A = V_A D_A / M_A$$

$$n_L = V_L D_L / M_L$$

$$m_g = V_L D_L \times 0.01$$

$$n_g = V_L D_L \times 0.01 / M_g$$

Applying $PV = nRT$,

$$P = \frac{nRT}{V}$$

$$\frac{P_g}{P_A} = \frac{n_g V_A T_2}{n_A V_g T_1} = \frac{100 \times 525}{2 \times 1.27 \times 298} = 69$$

The partial pressure of water vapor is still about 40 bar, because the concentration of the soluble content in water is very low at this temperature (Raoult's law). Therefore, the total pressure could be 69 + 40 = 109 bar.

To characterize the crack nucleation and development of the graphene under interior gas pressure, we adopt the extended finite element method to simulate the growth of the crack in the graphene. XFEM is a numerical technique that extends the classical finite element method (FEM) approach by extending the solution space for solutions to differential equations with discontinuous functions. A key advantage of XFEM is that in such problems the finite element mesh does not need to be updated to track the crack path,[45] while FEM has to use mesh refinement to solve such problems.

We first construct the graphene−cell−SiO_2 system shown in Figure 4a and equilibrate the system using molecular dynamics simulation. To determine where the crack will be nucleated under interior gas pressure, we can apply a uniform pressure on graphene, as shown in Figure 4b. From the FEM calculation results, we find that the location where curvature of the height profile is zero bears the maximum principle stress. We then simulate the evolution of the crack using XFEM; the crack evolution at different time points is shown in Figure 4c. To demonstrate the growth of the crack, we also plot the PHILSM (the level set value of friction angle) contour of the crack tip at different time points. The movie showing the development of the crack can be found in Supporting Movie S4.

Atomistic Molecular Dynamics Simulations (AMD). These were performed with NAMD[46] and the CHARMM force field (CHARMM general force field, CHARMM36 lipid force field),[47−49] using the Langevin dynamics (time step of 2 fs, temperature of T = 300 K, and damping coefficient of γ_{Lang} = 0.1 ps^{-1}). Nonbonding interactions had a cutoff distance of d = 10 Å, and long-range electrostatic interactions were calculated by the PME[50] method (periodic boundary conditions). In Figure 4d, we show the stabilized atomic level structure of the wrinkled graphene on the bacterial cell obtained after 2 ns of steered MD simulations. First, we used CHARMM-GUI[51−54] to prepare the lipid bilayer (80 × 550 $Å^2$) composed of two different types of bacterial phospholipids, PMPE (neutral) and PVPG (negatively charged), in a 2:3 ratio, respectively. We have also prepared the peptidoglycan layer (thickness 25−30 Å, 100 × 600 $Å^2$). The layer was composed of linear chains of two amino sugars, namely *N*-acetylglucosamine (GlcNAc) and *N*-acetylemuramic acid (MurNAc). MurNAc was joined with an amino acid chain containing alanine, glutamine, lysine, and alanine, and these tetrapeptides were interbridged with five glysin molecules. We have separately equilibrated (5 ns) in an NPT ensemble the hydrated lipid bilayer and the peptidoglycan layer with a graphene layer adsorbed on its top. Then, we have combined these subsystems and modeled them as a whole with steered MD simulations (forced), while applying a damping coefficient of 50 ps^{-1}. The force was applied on all atoms except hydrogen. Its value was proportional (k = 0.1 pN) to the square of the distance from the system center (length 600 Å). The force was acting from the outer surface (graphene) toward the inner surface (lipid bilayer) of the cell wall, and at each point its direction was normal to the graphene surface.

ASSOCIATED CONTENT

Supporting Information

The Supporting Information is available free of charge on the ACS Publications website at DOI: 10.1021/acsnano.6b03214.

Section 1. Calculation of average wavelength from AFM image; Section 2. Calculation of average wavelength from FESEM images; Section 3. Calculation of average wavelength and average amplitude in model; Section 4. Calculation of Strain in graphene from 2D peak shifts in Raman spectroscopy (PDF)

Graphene flap-valve and space bag (MOV)

The graphene coating process on a bacteria lying on the substrate (MOV)

Wrinkle development in the graphene−bacteria contact after the bacteria shrinks (MOV)

XFEM for crack formation process (MOV)

AUTHOR INFORMATION

Corresponding Author

*E-mail (V. Berry): vikasb@uic.edu.

Author Contributions

V.B. conceived and directed the project, S.D. conducted most of the experiments, Z.X., E.G., and Y.W. conducted coarse-grained simulations, while P.K. and S.S. performed molecular dynamics simulations. S.D., T.S.S., and S.B. performed characterizations. All authors contributed toward writing the manuscript.

Notes

The authors declare no competing financial interest.

ACKNOWLEDGMENTS

V.B. thanks the support from start-up funds from the University of Illinois at Chicago and partial support from NSF (CMMI-1054877, CMMI-0939523, and CMMI-1030963) and Office of Naval Research (Grant-N000141110767). The CGMD and XFEM parts of the work are supported by the National Natural Science Foundation of China through Grant 11222217. The work of P.K. was supported by the NSF DMR Grant No. 1309765 and by the ACS PRF Grant No. 53062-ND6. Thanks to Namrita V. Berry for the help with the Ziploc video. Thanks to Prof. Vivek Sharma for useful discussions.

REFERENCES

(1) Meyer, J. C.; Geim, A. K.; Katsnelson, M. I.; Novoselov, K. S.; Booth, T. J.; Roth, S. The Structure of Suspended Graphene Sheets. *Nature* **2007**, *446*, 60−63.

(2) Bao, W.; Miao, F.; Chen, Z.; Zhang, H.; Jang, W.; Dames, C.; Lau, C. N. Controlled Ripple Texturing of Suspended Graphene and Ultrathin Graphite Membranes. *Nat. Nanotechnol.* **2009**, *4*, 562−566.

(3) Zang, J.; Ryu, S.; Pugno, N.; Wang, Q.; Tu, Q.; Buehler, M. J.; Zhao, X. Multifunctionality and Control of the Crumpling and Unfolding of Large-Area Graphene. *Nat. Mater.* **2013**, *12*, 321−325.

(4) Zhu, W.; Low, T.; Perebeinos, V.; Bol, A. A.; Zhu, Y.; Yan, H.; Tersoff, J.; Avouris, P. Structure and Electronic Transport in Graphene Wrinkles. *Nano Lett.* **2012**, *12*, 3431−3436.

(5) Deng, S.; Berry, V. Wrinkled, Rippled and Crumpled Graphene: An Overview of Formation Mechanism, Electronic Properties, and Applications. *Mater. Today* **2016**, *19*, 197−212.

DOI: 10.1021/acsnano.6b03214
ACS Nano 2016, 10, 8403−8412

(6) Yan, W.; He, W.-Y.; Chu, Z.-D.; Liu, M.; Meng, L.; Dou, R.-F.; Zhang, Y.; Liu, Z.; Nie, J.-C.; He, L. Strain and Curvature Induced Evolution of Electronic Band Structures in Twisted Graphene Bilayer. *Nat. Commun.* **2013**, *4*10.1038/ncomms3159
(7) Eun-Ah, K.; Neto, A. H. C. Graphene as an Electronic Membrane. *Europhysics Lett.* **2008**, *84*, 57007.
(8) Jung, S.; Rutter, G. M.; Klimov, N. N.; Newell, D. B.; Calizo, I.; Hight-Walker, A. R.; Zhitenev, N. B.; Stroscio, J. A. Evolution of Microscopic Localization in Graphene in a Magnetic Field from Scattering Resonances to Quantum Dots. *Nat. Phys.* **2011**, *7*, 245−251.
(9) Kvashnin, A. G.; Sorokin, P. B.; Yakobson, B. I. Flexoelectricity in Carbon Nanostructures: Nanotubes, Fullerenes, and Nanocones. *J. Phys. Chem. Lett.* **2015**, *6*, 2740−2744.
(10) Wang, Q. H.; Jin, Z.; Kim, K. K.; Hilmer, A. J.; Paulus, G. L. C.; Shih, C.-J.; Ham, M.-H.; Sanchez-Yamagishi, J. D.; Watanabe, K.; Taniguchi, T.; Kong, J.; Jarillo-Herrero, P.; Strano, M. S. Understanding and Controlling the Substrate Effect on Graphene Electron-Transfer Chemistry *via* Reactivity Imprint Lithography. *Nat. Chem.* **2012**, *4*, 724−732.
(11) Mohanty, N.; Berry, V. Graphene-Based Single-Bacterium Resolution Biodevice and DNA Transistor: Interfacing Graphene Derivatives with Nanoscale and Microscale Biocomponents. *Nano Lett.* **2008**, *8*, 4469−4476.
(12) Huang, Y.; Dong, X.; Liu, Y.; Li, L.-J.; Chen, P. Graphene-Based Biosensors for Detection of Bacteria and Their Metabolic Activities. *J. Mater. Chem.* **2011**, *21*, 12358−12362.
(13) Sreeprasad, T. S.; Nguyen, P.; Alshogeathri, A.; Hibbeler, L.; Martinez, F.; McNeil, N.; Berry, V. Graphene Quantum Dots Interfaced with Single Bacterial Spore for Bio-Electromechanical Devices: A Graphene Cytobot. *Sci. Rep.* **2015**, *5*.913810.1038/srep09138
(14) Cohen-Karni, T.; Qing, Q.; Li, Q.; Fang, Y.; Lieber, C. M. Graphene and Nanowire Transistors for Cellular Interfaces and Electrical Recording. *Nano Lett.* **2010**, *10*, 1098−1102.
(15) Janata, J. Graphene Bio-Field-Effect Transistor Myth. *ECS Solid State Lett.* **2012**, *1*, M29−M31.
(16) McFarlane, I. R.; Lazzari-Dean, J. R.; El-Naggar, M. Y. Field Effect Transistors Based on Semiconductive Microbially Synthesized Chalcogenide Nanofibers. *Acta Biomater.* **2015**, *13*, 364−373.
(17) Mohanty, N.; Fahrenholtz, M.; Nagaraja, A.; Boyle, D.; Berry, V. Impermeable Graphenic Encasement of Bacteria. *Nano Lett.* **2011**, *11*, 1270−1275.
(18) Mohanty, N.; Moore, D.; Xu, Z.; Sreeprasad, T. S.; Nagaraja, A.; Rodriguez, A. A.; Berry, V. Nanotomy-Based Production of Transferable and Dispersible Graphene Nanostructures of Controlled Shape and Size. *Nat. Commun.* **2012**, *3*, 844.
(19) Berry, V. Impermeability of Graphene and Its Applications. *Carbon* **2013**, *62*, 1−10.
(20) Lee, C.; Wei, X.; Kysar, J. W.; Hone, J. Measurement of the Elastic Properties and Intrinsic Strength of Monolayer Graphene. *Science* **2008**, *321*, 385−388.
(21) Tortora, G. J.; Funke, B. R.; Case, C. L. *Microbiology: An Introduction*; Pearson Education, 2016; pp 80−84.
(22) Castle, J. E.; Zhdan, P. A. Characterization of Surface Topography by SEM and SFM: Problems and Solutions. *J. Phys. D: Appl. Phys.* **1997**, *30*, 722.
(23) Irina, A.; Stoica, J.; Hulubei, C. *Semi-Alicyclic Polyimides: Insights into Optical Properties and Morphology Patterning Approaches for Advanced Technologies* **2012**, DOI: 10.5772/53607.
(24) Ni, Z. H.; Yu, T.; Lu, Y. H.; Wang, Y. Y.; Feng, Y. P.; Shen, Z. X. Uniaxial Strain on Graphene: Raman Spectroscopy Study and Band-Gap Opening. *ACS Nano* **2008**, *2*, 2301−2305.
(25) Melanitis, N.; Tetlow, P. L.; Galiotis, C. Characterization of PAN-Based Carbon Fibres with Laser Raman Spectroscopy. *J. Mater. Sci.* **1996**, *31*, 851−860.
(26) Lee, J. E.; Ahn, G.; Shim, J.; Lee, Y. S.; Ryu, S. Optical Separation of Mechanical Strain from Charge Doping in Graphene. *Nat. Commun.* **2012**, *3*, 1024.
(27) Reich, S.; Jantoljak, H.; Thomsen, C. Shear Strain in Carbon Nanotubes under Hydrostatic Pressure. *Phys. Rev. B: Condens. Matter Mater. Phys.* **2000**, *61*, R13389−R13392.
(28) An, Y. H.; Friedman, R. J. Concise Review of Mechanisms of Bacterial Adhesion to Biomaterial Surfaces. *J. Biomed. Mater. Res.* **1998**, *43*, 338−348.
(29) Cerda, E.; Mahadevan, L. Geometry and Physics of Wrinkling. *Phys. Rev. Lett.* **2003**, *90*, 74302.
(30) Huang, J.; Juszkiewicz, M.; de Jeu, W. H.; Cerda, E.; Emrick, T.; Menon, N.; Russell, T. P. Capillary Wrinkling of Floating Thin Polymer Films. *Science* **2007**, *317*, 650−653.
(31) Schelling, P. K.; Keblinski, P. Thermal Expansion of Carbon Structures. *Phys. Rev. B: Condens. Matter Mater. Phys.* **2003**, *68*, 35425.
(32) Chen, X.; Hutchinson, J. W. Herringbone Buckling Patterns of Compressed Thin Films on Compliant Substrates. *J. Appl. Mech.* **2004**, *71*, 597−603.
(33) Jiang, H.; Khang, D.-Y.; Song, J.; Sun, Y.; Huang, Y.; Rogers, J. A. Finite Deformation Mechanics in Buckled Thin Films on Compliant Supports. *Proc. Natl. Acad. Sci. U. S. A.* **2007**, *104*, 15607−15612.
(34) Lan, G.; Wolgemuth, C. W.; Sun, S. X. Z-Ring Force and Cell Shape during Division in Rod-like Bacteria. *Proc. Natl. Acad. Sci. U. S. A.* **2007**, *104*, 16110−16115.
(35) Yin, J.; Cao, Z.; Li, C.; Sheinman, I.; Chen, X. Stress-Driven Buckling Patterns in Spheroidal Core/shell Structures. *Proc. Natl. Acad. Sci. U. S. A.* **2008**, *105*, 19132−19135.
(36) Plimpton, S. Fast Parallel Algorithms for Short-Range Molecular Dynamics. *J. Comput. Phys.* **1995**, *117*, 1−19.
(37) Xu, Z.; Buehler, M. J. Geometry Controls Conformation of Graphene Sheets: Membranes, Ribbons, and Scrolls. *ACS Nano* **2010**, *4*, 3869−3876.
(38) MacKerell, A. D.; Banavali, N.; Foloppe, N. Development and Current Status of the CHARMM Force Field for Nucleic Acids. *Biopolymers* **2000**, *56*, 257−265.
(39) Awasthi, A. P.; Lagoudas, D. C.; Hammerand, D. C. Modeling of Graphene−polymer Interfacial Mechanical Behavior Using Molecular Dynamics. *Modell. Simul. Mater. Sci. Eng.* **2009**, *17*, 015002.
(40) Ni, B.; Lee, K.-H.; Sinnott, S. B. A Reactive Empirical Bond Order (REBO) Potential for Hydrocarbon−Oxygen Interactions. *J. Phys.: Condens. Matter* **2004**, *16*, 7261−7275.
(41) Brooks, B. R.; Bruccoleri, R. E.; Olafson, B. D.; States, D. J.; Swaminathan, S.; Karplus, M. CHARMM: A Program for Macromolecular Energy, Minimization, and Dynamics Calculations. *J. Comput. Chem.* **1983**, *4*, 187−217.
(42) Hockney, R. W.; Eastwood, J. W. Computer Simulation Using Particles. *SIAM Rev.* **1988**, *25*, 540.
(43) Das, S.; Lahiri, D.; Agarwal, A.; Choi, W. Interfacial Bonding Characteristics between Graphene and Dielectric Substrates. *Nanotechnology* **2014**, *25*, 045707.
(44) Koenig, S. P.; Boddeti, N. G.; Dunn, M. L.; Bunch, J. S. Ultrastrong Adhesion of Graphene Membranes. *Nat. Nanotechnol.* **2011**, *6*, 543−546.
(45) Moës, N.; Dolbow, J.; Belytschko, T. A Finite Element Method for Crack Growth without Remeshing. *Int. J. Numer. Meth. Engng* **1999**, *46*, 131−150.
(46) Phillips, J. C.; Braun, R.; Wang, W.; Gumbart, J.; Tajkhorshid, E.; Villa, E.; Chipot, C.; Skeel, R. D.; Kalé, L.; Schulten, K. Scalable Molecular Dynamics with NAMD. *J. Comput. Chem.* **2005**, *26*, 1781−1802.
(47) Yu, W.; He, X.; Vanommeslaeghe, K.; MacKerell, A. D. Extension of the CHARMM General Force Field to Sulfonyl-Containing Compounds and Its Utility in Biomolecular Simulations. *J. Comput. Chem.* **2012**, *33*, 2451−2468.
(48) Feller, S. E.; Yin, D.; Pastor, R. W.; MacKerell, A. D. Molecular Dynamics Simulation of Unsaturated Lipid Bilayers at Low Hydration: Parameterization and Comparison with Diffraction Studies. *Biophys. J.* **1997**, *73*, 2269−2279.
(49) Klauda, J. B.; Venable, R. M.; Freites, J. A.; O'Connor, J. W.; Tobias, D. J.; Mondragon-Ramirez, C.; Vorobyov, I.; MacKerell, A. D.;

DOI: 10.1021/acsnano.6b03214
ACS Nano 2016, 10, 8403−8412

Pastor, R. W. Update of the CHARMM All-Atom Additive Force Field for Lipids: Validation on Six Lipid Types. *J. Phys. Chem. B* **2010**, *114*, 7830−7843.
(50) Darden, T.; York, D.; Pedersen, L. Particle Mesh Ewald: An N·log(N) Method for Ewald Sums in Large Systems. *J. Chem. Phys.* **1993**, *98*, 10089−10092.
(51) Jo, S.; Lim, J. B.; Klauda, J. B.; Im, W. CHARMM-GUI Membrane Builder for Mixed Bilayers and Its Application to Yeast Membranes. *Biophys. J.* **2009**, *97*, 50−58.
(52) Wu, E. L.; Cheng, X.; Jo, S.; Rui, H.; Song, K. C.; Dávila-Contreras, E. M.; Qi, Y.; Lee, J.; Monje-Galvan, V.; Venable, R. M.; Klauda, J. B.; Im, W. CHARMM-GUI Membrane Builder toward Realistic Biological Membrane Simulations. *J. Comput. Chem.* **2014**, *35*, 1997−2004.
(53) Jo, S.; Kim, T.; Iyer, V. G.; Im, W. CHARMM-GUI: A Web-Based Graphical User Interface for CHARMM. *J. Comput. Chem.* **2008**, *29*, 1859−1865.
(54) Jo, S.; Kim, T.; Im, W. Automated Builder and Database of Protein/Membrane Complexes for Molecular Dynamics Simulations. *PLoS One* **2007**, *2*, e880.

DOI: 10.1021/acsnano.6b03214
ACS Nano 2016, 10, 8403−8412